Probing Interfacial Characteristics of Rubrene/Pentacene and Pentacene/Rubrene Bilayers with Soft X-Ray Spectroscopy

J. H. Seo,[†] T. M. Pedersen,[‡] G. S. Chang,*[,‡] A. Moewes,[‡] K.-H. Yoo,[†] S. J. Cho,[§] and C. N. Whang*[,†]

Institute of Physics and Applied Physics, Yonsei University, Seoul, 120-749, Korea, Department of Physics and Engineering Physics, University of Saskatchewan, Saskatchewan, SK S7N 5E2, Canada, and Department of Physics, Kyungsung University, Busan, 608-736, Korea

Received: January 15, 2007; In Final Form: June 6, 2007

The electronic structure of rubrene/pentacene and pentacene/rubrene bilayers has been investigated using soft X-ray absorption spectroscopy, resonant X-ray emission spectroscopy, and density-functional theory calculations. X-ray absorption and emission measurements reveal that it has been possible to alter the lowest unoccupied and the highest occupied molecular orbital states of rubrene in rubrene/pentacene bilayer. In the reverse case, one gets p* molecular orbital states originating from the pentacene layer. Resonant X-ray emission spectra suggest a reduction in the hole-transition probabilities for the pentacene/rubrene bilayer in comparison to reference pentacene layer. For the rubrenepentacene structure, the hole-transition probability shows an increase in comparison to the rubrene reference. We also determined the energy level alignment of the pentacene−rubrene interface by using X-ray and ultraviolet photoelectron spectroscopy. From these comparisons, it is found that the electronic structure of the pentacene−rubrene interface has a strong dependence on interface characteristics which depends on the order of the layers used.

1. Introduction

Thin-film transistors (TFTs) based on organic semiconductors have garnered strong interest due to their compatibility with plastic substrates, which makes them applicable in flexible displays, smart cards, and printable electronic circuits.[1−3] In the near future, one can expect to see pentacene, rubrene, and other organic semiconductors, complementing traditional inorganic semiconductors in electronic applications. Rubrene ($C_{42}H_{28}$) has especially shown promise for use as a doping layer for organic light-emitting devices (OLEDs) and as a channel material in organic field-effect transistors (OFETs).[3−6] Since rubrene single-crystal FETs demonstrate a higher field-effect mobility (up to 20 $cm^2\ V^{-1}\ s^{-1}$) than those made from anthracene ($C_{14}H_{10}$), tetracene ($C_{18}H_{12}$), and pentacene ($C_{22}H_{14}$) single crystals, enormous effort has gone into achieving a high carrier mobility in OTFTs based on rubrene thin films. However, the fabrication of rubrene-based thin-film FETs (TFFETs) with the necessary electronic properties has been hampered by the fact that a thin layer of rubrene with high crystallinity is extremely difficult to synthesize with organic molecular beam deposition (OMBD) techniques.[7−9]

Recently, Itaka et al. investigated the buffer-layer effect on growth characteristics of rubrene thin films and reported that when rubrene is deposited onto a pentacene buffer layer which resides on a sapphire substrate, the surface roughness of the rubrene thin film is clearly improved.[10,11] On the other hand, our previous research has shown that the crystallinity and electrical properties of rubrene-based TFFETs significantly depend on the layer ordering of the pentacene.[12] High-quality rubrene crystalline films with an orthorhombic structure were obtained by depositing rubrene onto a pentacene buffer layer (rubrenepentacene), while reversing the deposition order (pentacene/rubrene) only resulted in an amorphous rubrene phase. This amorphous phase of rubrene on SiO_2 substrate is not surprising, as shown by others before.[7−9,13] The TFFET device performance based on rubrene/pentacene bilayers was far superior to the opposite arrangement of pentacene on rubrene. These results reflect that the electrical properties of rubrene-based TFFETs are affected by the interfacial electronic structure between rubrene and pentacene.

In this paper, we extensively investigate changes in the electronic structure at the interface of the rubrene and pentacene layers using soft X-ray absorption and emission spectroscopy in order to understand the mechanism of interface formation for both the rubrene/pentacene and pentacene/rubrene bilayers. The nature of the chemical bonding and charge transfer at the interface was investigated using X-ray photoemission spectroscopy (XPS). The valence band electronic structure, work function, and ionization potential were examined via ultraviolet photoelectron spectroscopy (UPS). Information concerning the interface dipole layer, band bending, and the offsets of the HOMO and LUMO levels at the interface, was obtained from valence band spectra and C 1s core level spectra.[14] Determining the alignment between the highest occupied molecular orbitals (HOMO) and the lowest unoccupied molecular orbitals (LUMO) at the interface allows characterizing how effectively the TFFETs may operate. We therefore have also studied the complete energy level diagram for the pentacene and rubrene systems.

2. Experimental Methods

Pentacene and rubrene organic layers were evaporated onto a heavily doped Si substrate possessing a 100 nm thick SiO_2

* To whom correspondence should be addressed. E-mails: gapsoo.chang@usask.ca; cnwhang@yonsei.ac.kr.
[†] Yonsei University.
[‡] University of Saskatchewan.
[§] Kyungsung University.

10.1021/jp070347p CCC: $37.00
Published on Web 07/21/2007

gate-oxide layer synthesized in a dry oxidation process. The two types of organic bilayers were prepared using thermal evaporation at a base pressure of 1×10^{-8} Torr. The prepared bilayers had the following structures: (a) 40 nm of rubrene deposited on top of 10 nm of pentacene (referred to as rubrene/pentacene) and (b) 40 nm of pentacene deposited on 10 nm of rubrene (pentacene/rubrene). The deposition rate was 0.1 Å/s in all depositions. The evaporation temperature was set at 160 °C for both pentacene and rubrene ensuring no thermal dissociation of the organic molecules. The temperature was measured at the outer surface of the Knudsen cell. After the growth of the organic bilayers, a 35 nm thick gold layer was thermally evaporated using a shadow mask to create the source and drain electrodes. The respective channel length and width for the electrodes were 50 μm and 1000 μm. Current−voltage ($I-V$) characteristics of the prepared OTFFETs were measured using a Keithley 4200-SCS source measurement unit. The unoccupied and occupied C 2*p* partial density of states (PDOS) were probed using X-ray absorption spectroscopy (XAS) and resonant X-ray emission spectroscopy (RXES), respectively. Spectroscopic measurements were conducted at beamline 8.0.1 of the Advanced Light Source at the Lawrence Berkeley National Laboratory. The excitation energy (E_{exc}) for resonant C $K\alpha$ (2p → 1s transition) emission spectra was selected to be 285.3 eV. All measured spectra are normalized to the number of photons falling on the sample monitored by a highly transparent gold mesh.

The XPS and UPS measurements were performed using a PHI 5700 spectrometer equipped with an Al Ka (1486.6 eV) tube and a He I (21.2 eV) discharge lamp. For XPS and UPS measurements, rubrene (or pentacene) was deposited on the pentacene (or rubrene) film in a stepwise manner. The working pressure was 2.0×10^{-9} Torr. The deposition rates for rubrene and pentacene were kept at 0.1 Å/s, and the nominal thickness was monitored with a calibrated quartz crystal monitor. After each deposition of either rubrene or pentacene, the sample was transferred to a separate XPS and UPS analysis chamber without breaking vacuum and the C 1s XPS and valence-band UPS spectra were immediately measured. The base pressure of the analysis chamber was maintained at 1×10^{-10} Torr. A sample bias of −15V was used in order to separate the sample and the high-binding-energy cutoff for the analyzer. The energy scale for each spectrum was calibrated using the Fermi level of a freshly deposited clean Au film.[14]

3. Results and Discussion

Figure 1 shows the $I-V$ characteristics of both a rubrene/pentacene-TFT (solid circles) and a pentacene/rubrene-TFT (open circles).[15] One can see that the rubrenepentacene-TFT exhibits superior electrical properties to the pentacene/rubrene-TFT. The drain current of the rubrene/pentacene-TFT (at $V_{ds} = -40$ V and $V_{gs} = -40$ V) is orders of magnitude larger than that of the pentacene/rubrene sample [Figure 1a]. From plots of transfer characteristics shown in Figure 1b and its inset, the on/off ratio and carrier mobilities (μ) at $V_{ds} = -30$ V are determined to be 10^3 and 0.6 cm^2/V·s for the rubrene/pentacene-TFT and 10 and 0.4×10^{-3} cm^2/V·s for the pentacene/rubrene-TFT, respectively. The observed output and transfer characteristics of OTFTs with differently ordered rubrene and pentacene layers suggest that the chemical interaction at the interface between rubrene and pentacene is significantly influenced by the deposition order. This leads us to further investigate changes in the electronic structure at the interface of the rubrene and pentacene layers.

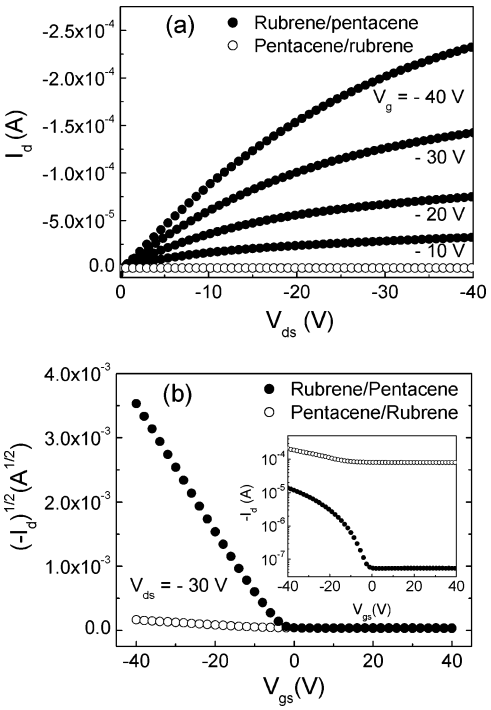

Figure 1. (a) Plots of drain current (I_d) vs drain voltage (V_{ds}) of rubrene on pentacene−OTFT (rubrene/pentacene = solid circles) and pentacene on rubrene (pentacene/rubrene = open circles) OTFT for various gate voltages (V_{gs}) and (b) the plots of the square root of I_d as a function of V_{gs} for $V_{ds} = -30$ V.[15] In the inset to (b) is plotted I_d vs V_{gs} for our OTFTs with $V_{ds} = -30$ V.

Figure 2a shows the C 1s XAS spectra of (i) the rubrene/pentacene bilayer, (ii) the rubrene reference sample, and (iii) the calculated carbon PDOS of the reference rubrene structure. The DFT calculations were carried out using the nonlocal hybrid Becke three-parameter Lee−Yang−Parr (B3LYP) function with the basis set of 6-31G after optimizing the geometries of rubrene and pentacene using the same method. More details can be found elsewhere.[16]

Rubrene is an aromatic molecule consisting of a tetracene backbone and four phenyl side groups. The geometry optimized rubrene molecule is structurally identical to the form rubrene takes in its molecular crystalline phase. This means that the tetracene backbone of the rubrene molecule is planar and does not exhibit chirality which is evident for the gas phase of the rubrene molecule.[13] As seen in Figure 2a, the π^* character for each of the films consists of two peaks located around 284 and 285.3 eV. The spectral intensity of the feature labeled A is the LUMO states for the rubrene molecule. The charge-density isosurfaces for the corresponding molecular states of rubrene are presented in Figure 2b. According to DFT calculations, the charge-density of LUMO states predominantly arises from the tetracene backbone in the rubrene molecule. On the other hand, the spectral weight from the peak labeled B in Figure 2a originates mainly from the four phenyl groups while that from the peak labeled C is caused by charge-density that is delocalized throughout the entire molecule. The different spectral contributions from the tetracene backbone and four phenyl side-groups are in good agreement with the measured spectra of rubrene using near-edge X-ray absorption fine structure (NEXAFS) spectroscopy.[9] Comparing the XAS spectra of rubrene and rubrene/pentacene films, the rubrene/pentacene bilayer exhibits a lower intensity for peak *A* than the rubrene single layer. This can be explained by considering the different molecular ordering of rubrene in the samples. During the XAS experiments the

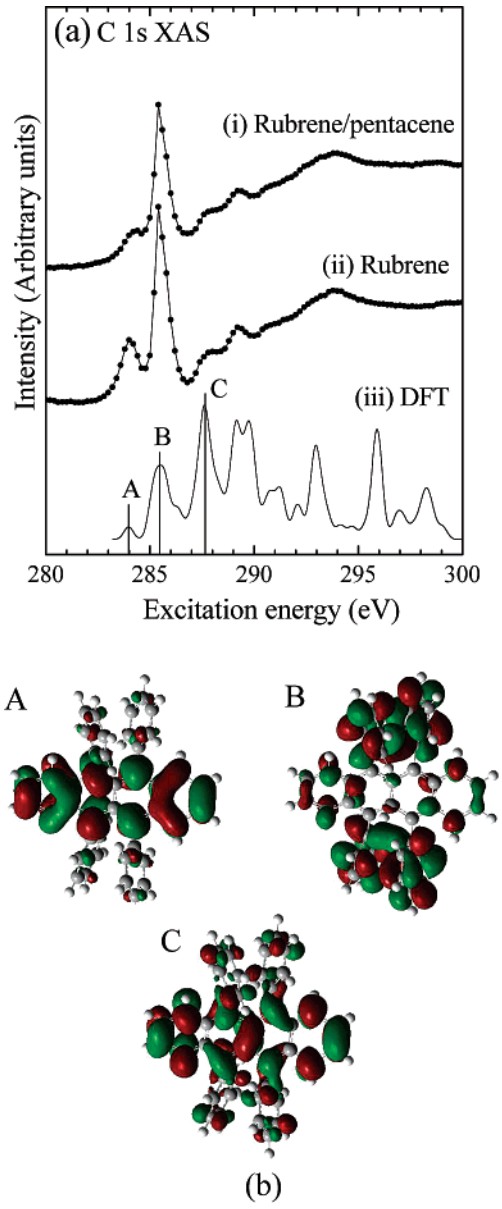

Figure 2. (a) C 1s XAS spectra of (i) rubrene/pentacene, (ii) rubrene reference, and (iii) calculated carbon partial density of states of rubrene using DFT. (b) Charge-density isosurfaces for the relevant molecular states of the rubrene molecule.

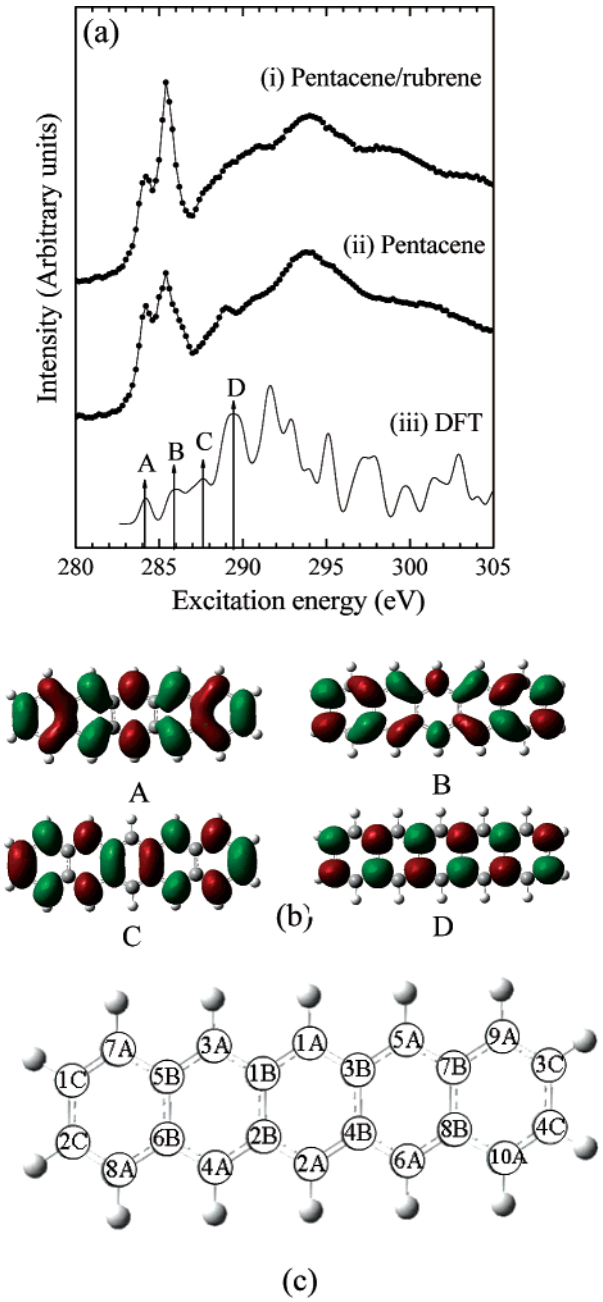

Figure 3. (a) C 1s XAS spectra of (i) pentacene/rubrene, (ii) pentacene reference, and (iii) calculated carbon partial density of states of pentacene using DFT. (b) Charge-density isosurfaces for the relevant molecular states of the pentacene molecule. (c) Schematic structure of the pentacene molecule optimized using DFT.

incident angle of linearly polarized X-rays was set to 30° with respect to the sample's normal direction and thus the XAS measurements mostly probe *p*-character of the molecule parallel to the sample surface. This means that if the rubrene molecules are lying flat on the substrate in an ordered phase (rubrene-pentacene bilayer), π^* orbitals perpendicular to the plane of tetracene are hardly probed by the incident X-rays. In the case of the rubrene reference sample, peaks *A* and *B* are both intense, suggesting that an amorphous phase is present in that sample. This is in accordance with our previous results from X-ray diffraction measurements.[12]

In comparison, Figure 3a shows the measured C 1s XAS spectra of (i) the pentacene/rubrene bilayer, (ii) the pentacene reference sample, and (iii) the calculated carbon PDOS of the pentacene reference structure. The charge-density isosurfaces for the relevant molecular states and the structural geometry of the pentacene molecule are shown in panels b and c, respectively, of Figure 3. The spectral weight from the peaks labeled A−D in Figure 3a can be assigned as π^*-molecular orbital states. Generally, π^* molecular orbital states are known to play a significant role in the conduction of charge carriers in organic materials due to their delocalized nature.[17] The spectral weight of the features labeled *A* and *B* in Figure 3a originate from the carbon atoms denoted 1A−6A and 1B−8B in the pentacene structure shown in Figure 3c, respectively. Likewise, the spectral weight from the peak labeled C originates from the C−C bonds denoted by 1B−4B and 1C−4C. Finally, the spectral weight from the peak labeled D arises from all 22 of the carbon atoms in the pentacene molecule. Contrary to the XAS spectra of the rubrene/pentacene bilayer and rubrene single layer, the C 1s XAS spectra of the pentacene/rubrene bilayer exhibits enhanced π^* features with respect to that of the pure pentacene layer. Therefore, from the intensity increases of peaks A−D, we surmise that the pentacene molecules are located in a random

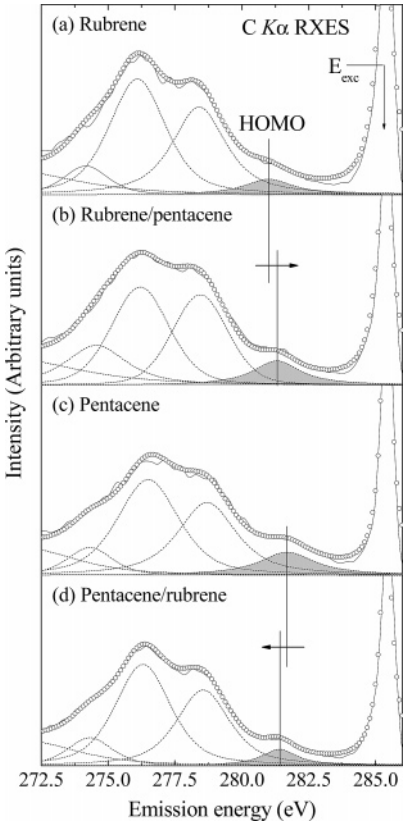

Figure 4. C Kα resonant XES spectra of (a) rubrene reference (line), (b) rubrenepentacene (circles), (c) pentacene reference (line), and (d) pentacene/rubrene (circles) taken at the excitation energy of 285.3 eV (at π^* resonance).

orientation stemming from the amorphous phase of the underlying rubrene surface. The pentacene single layer in contrast is a polycrystalline phase.[12]

In addition to C 1s XAS spectra, we also measured occupied C 2p valence states of our samples using resonant X-ray emission spectroscopy. The C *K*α RXES spectra of the rubrene reference sample and the rubrene/pentacene bilayer (excited at π^*-resonance in Figure 3a) are shown in panels a and b, respectively, of Figure 4. Setting the excitation energy to 285.3 eV gives us the valence band emission spectra located between 272 and 284 eV, with their corresponding σ and π molecular orbital states occurring at 272−276 and 276−284 eV respectively. To investigate changes in the HOMO states in detail, the RXES spectra were fitted using Voigt functions. Since a rubrene molecule consists of phenyl rings as building blocks, the spectra were fitted by considering the molecular orbitals of phenyl ring. The five peaks at 281, 278.4, 276.1, 274.2, and 271.2 in the RXES spectra correspond to X-ray transitions involving the $1e_{1g}$, $3e_{2g}+1a_{2u}$, $3e_{1u}+1b_{2u}+2b_{1u}$, $3a_{1g}$, and $2e_{2g}$ molecular orbitals, respectively.[18] The results clearly reveal that the HOMO states ($1e_{1g}$ orbital) of our devices depend on the arrangement of rubrene and pentacene layers. The spectral weight of HOMO states (shaded peak) for the rubrene/pentacene bilayer increases with respect to that of the rubrene reference layer. In addition, the rubrene/pentacene heterostructure has a lower HOMO energy position (higher emission energy) than that of the rubrene single layer (see arrow in Figure 4). These results suggest that hole transitions in the rubrene/pentacene bilayer occurs more readily in comparison to the rubrene single layer.

C *K*α RXES spectra of the pentacene reference sample and the pentacenerubrene bilayer are presented in panels c and d,

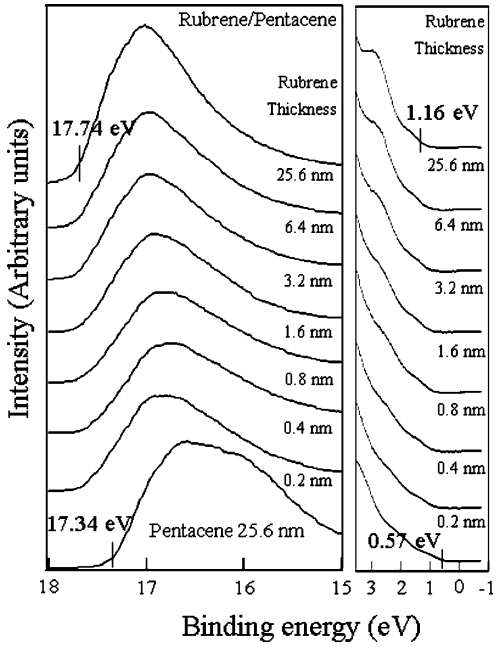

Figure 5. LHS: UPS spectra in the high binging energy cutoff region of rubrene on pentacene (25.6 nm) for various rubrene thicknesses. RHS:HOMO region for the rubrene layers (with respect to the Fermi level, E_F). The intensity is normalized allowing a better comparison between spectra.

respectively, of Figure 4. In contrast to the results for both the single rubrene layer and rubrene/pentacene bilayer, the pentacene/rubrene heterostructure exhibits a higher spectral intensity and a lower energy position for the HOMO states than those of the pentacene reference sample. One can therefore expect the hole transition rate for the pentacene/rubrene bilayer to decrease in comparison to the pentacene single layer reference sample. These results agree well with the superior output and transfer characteristics of the rubrene/pentacene-TFT compared to those of the pentacene/rubrene-TFT shown in Figure 1.

To further understand how the deposition order affects the rubrene-OTFT device performance, the electronic structure at the interface between the pentacene and rubrene layers was investigated by measuring C 1s XPS and valence-band UPS spectra of both rubrene and pentacene. Figure 5 shows UPS spectra taken for various rubrene layer thicknesses to determine the alignment of the HOMO level at the interface. The spectra were collected along the surface normal direction with an incidence angle of 30°. On the left side of Figure 5, the high binding energy cutoff position shifts toward higher biding energy as rubrene is deposited onto pentacene (25.6 nm). A 25.6 nm thick rubrene layer exhibits a 0.4 eV higher cutoff value than that of the bare pentacene surface. This shift suggests a lower vacuum level for rubrene than that of pentacene as the vacuum level of the film can be determined by linear extrapolation of the cutoff level for secondary electrons. This is done on the high-binding energy side of the UPS spectra.[14]

This shift in the high-binding energy cutoff value can be attributed to an interface dipole layer between rubrene and pentacene. The redistribution of electrons at the interface between rubrene and pentacene occurs as rubrene is deposited on pentacene. The right-hand side of Figure 5 shows the evolution of the HOMO onset during growth of the rubrene layer on pentacene (25.6 nm). After depositing rubrene, the emission from the pentacene layer becomes suppressed, and the spectrum changes to that of rubrene. Comparing the shift in the HOMO onset of rubrene to the Fermi level of Au gives us

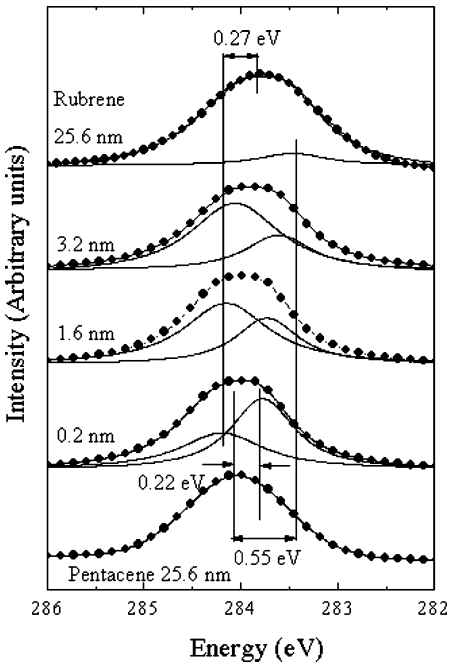

Figure 6. XPS spectra of the C 1s core levels as a function of rubrene coverage on the pentacene layer.

the relative position of the HOMO level. Based on the 25.6 nm thick rubrene layer, the HOMO onset was determined to be 1.16 eV below the Au Fermi level.

Figure 6 shows the C 1s XPS spectra for the samples with rubrene grown on pentacene. The bottom of the figure starts with the pentacene reference sample and continues with the spectra for successively thicker layers of rubrene that were deposited onto pentacene. At the maximum rubrene coverage of 25.6 nm, the C 1s peak for pentacene shifted 0.55 eV toward lower binding energy. This indicates that the charge redistribution occurs from pentacene to rubrene (in the pentacene region). Conversely the C 1s peak of rubrene emerges after only 0.2 nm of rubrene is deposited. The peak shift reaches a maximum of 0.27 eV toward the low binding energy side for the rubrene (25.6 nm)/pentacene (25.6 nm) structure. This is clear evidence that band bending occurs on both sides of the pentacene (0.55 eV) and rubrene (0.49 eV) interface.

On the basis of our analysis of UPS and XPS spectra, we can characterize the interfacial electronic structure of rubrene on the pentacene underlayer. The ionization potentials (IPs) of pentacene and rubrene are determined using the incident photon energy of 21.2 eV, the high binding cutoff energy (E_{cutoff}), and the onset energy of the HOMO level (E_{HOMO}) determined from the UPS measurements. According to these values, the IPs of pentacene and rubrene are 4.43 and 4.62 eV, respectively. In addition, the energy of the LUMO levels are found to be 1.63 eV for pentacene and 1.14 eV for rubrene by using the known optical band-gaps (2.2 eV for pentacene[19] and 2.3 eV for rubrene[20]). The barrier height for hole injection from pentacene to rubrene is found to be 1.14 eV. The above results are summarized in the energy scheme of Figure 7a, where the energy levels of the rubrene/pentacene interface are shown. For the pentacene/rubrene structure, the electronic structure values are derived from similar analysis of UPS and XPS spectra (not shown) and Figure 7b displays the obtained energy level alignment of the pentacene/rubrene interface.

Comparing the energy level diagrams for the rubrene/pentacene and pentacenerubrene heterostructures clearly shows differing electronic properties for the two systems. The HOMO

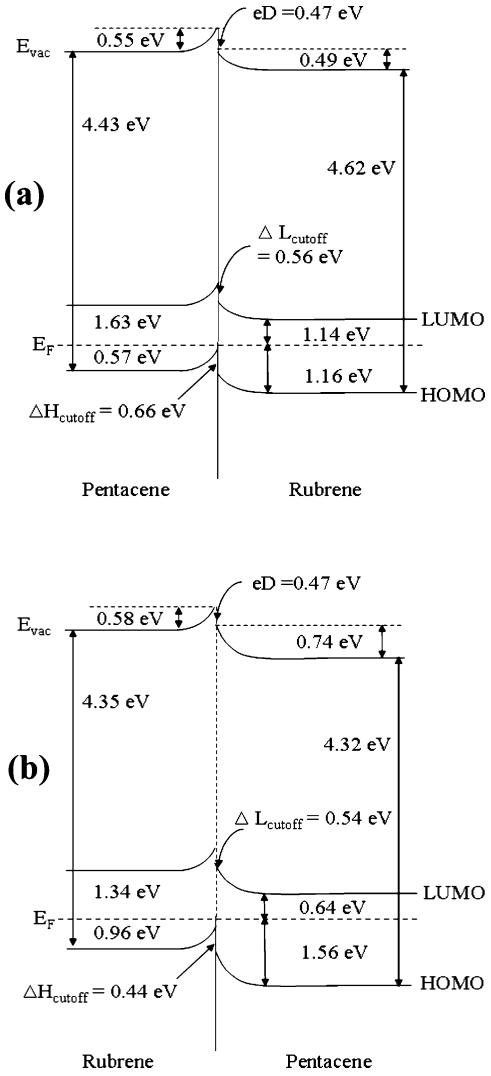

Figure 7. Energy level diagrams of the (a) rubrene/pentacene and (b) pentacenerubrene interface.

offset at the rubrene/pentacene interface increases as the rubrene is deposited on the pentacene layer. Quantifying these results yields a value of 0.47 eV for the interface dipole energy (eD) between the rubrene and pentacene layers. This indicates that the deposition sequence affects the molecular level alignment at the interface. The hole injection barrier of pentacene/rubrene [Figure 7a] is lower than that of rubrene/pentacene (based on a common Fermi level). As a result the rubrene/pentacene structure possesses superior electrical characteristics in comparison to the pentacene/rubrene structure. We suggest that electrical properties for rubrene/pentacene-TFFETs are dependent not only on chemical reactions at the interface of dissimilar layers but on the energy level alignment at that interface.

4. Conclusions

In conclusion, we have investigated the changes that occur in the electronic structure of rubrene/pentacene-TFFETs depending on the deposition order of the heterostructure layers. This was accomplished by combining soft X-ray spectroscopy with theoretical calculations based on density functional theory. According to results from X-ray absorption and emission spectroscopy, inserting a pentacene layer between a layer of rubrene and SiO_2 can increase the hole-transition probabilities, which results in the enhancement of charge transport characteristics of OTFFETs. However, when a rubrene layer is inserted

between the pentacene and SiO_2 layers, we find that there is a reduction in the hole transition probability. We also determined the energy level alignment of the pentacene−rubrene interface from X-ray and ultraviolet photoelectron spectroscopy. The measured HOMO/LUMO cutoffs and ionization potentials show different energy level alignments of rubrene/pentacene in comparison to pentacene/rubrene. These results reveal that the electronic structure of the pentacene−rubrene interface has a strong dependence on interface characteristics which in turn depend on the layering order used.

Acknowledgment. This work was supported by the Brain Korea 21 project of the Korea Research Foundation, and the Korea Science and Engineering Foundation through the National Core Research Center for Nanomedical Technology. We gratefully acknowledge the Natural Sciences and Engineering Research Council of Canada and the Canada Research Chair program. S. J. Cho acknowledges support from Kyungsung University in 2005.

References and Notes

(1) Baude, P. F.; Ender, D. A.; Haase, M. A.; Kelly, T. W.; Muyres, D. V.; Theiss, S. D. *Appl. Phys. Lett.* **2003**, *82*, 3964−3966.

(2) Brown, A. R.; Pomp, A.; Hart, C. M.; Leeuw, D. M. *Science* **1995**, *270*, 972−974.

(3) Dimitrakopoulos, C. D.; Malenfant, P. R. L. *Adv. Mater*. **2003**, *14*, 99−117.

(4) Menard, E.; Podzorov, V.; Hur, S.-H.; Gaur, A.; Gershenson, M. E.; Rogers, J. A. *Adv. Mater*. **2004**, *16*, 2097−2101.

(5) Boer, R. W. I.; Gershenson, M. E.; Morpurgo, A. F.; Podzorov, V. *Phys. Status Solidi A* **2004**, *201*, 1302−1331.

(6) Goldmann, C.; Krellner, C.; Pernstich, K. P.; Haas, S.; Gundlach, D. J.; Batlogg, B. *J. Appl. Phys.* **2006**, *99*, 034507.

(7) Käfer, D.; Witte, G. *Phys. Chem. Chem. Phys*. **2005**, *7*, 2850−2853.

(8) Kowarik, S.; Gerlach, A.; Sellner, S.; Schreiber, F.; Pflaum, J.; Cavalcanti, L.; Konovalov, O. *Phys. Chem. Chem. Phys*. **2006**, *8*, 1834−1836.

(9) Käfer, D.; Ruppel, L.; Witte, G. Wöll. Ch. *Phys. Rev. Lett*. **2005**, *95*, 166602.

(10) Itaka, K.; Yamashiro, M.; Yamaguchi, J.; Yaginuma, S.; Haemori, M.; Koinuma, H. *Appl. Surf. Sci*. **2006**, *252*, 2562−2567.

(11) Haemori, M.; Yamaguchi, J.; Yaginuma, S.; Itaka, K.; Koinuma, H. *Jpn. J. Appl. Phys*. **2005**, *44*, 3740−3742.

(12) Seo, J. H.; Park, D. S.; Cho, S. W.; Kim, C. Y.; Jang, W. C.; Whang, C. N.; Yoo, K.-H.; Chang, G. S.; Pedersen, T.; Moewes, A.; Chae, K. H.; Cho, S. J. *Appl. Phys. Lett*. **2006**, *89*, 163505.

(13) (a) Blüm, M.-C.; _avar, E.; Pivetta, M.; Patthey, F.; Schneider, W.-D. *Angew. Chem. Int. Ed.* **2005**, *44*, 5334−5337. (b) Blüm, M.-C.; Pivetta, M.; Patthey, F.; Schneider, W.-D. *Phys. Rev. B* **2006**, *73*, 195409.

(14) Seo, J. H.; Kang, S. J.; Kim, C. Y.; Yoo, K.-H.; Whang, C. N. *J. Phys.: Condens. Matter* **2006**, *18*, S2055−S2060.

(15) The I_d-V_{ds} and square roots of I_d-V_{gs} plots are reused with permission from Seo, J. H.; Park, D. S.; Cho, S. W.; Kim, C. Y.; Jang, W. C.; Whang, C. N.; Yoo, K.-H.; Chang, G. S.; Pedersen, T.; Moewes, A.; Chae, K. H.; Cho, S. J. *Appl. Phys. Lett*. **2006**, *89*, 163505.

(16) Seo, J. H.; Kim, C. Y.; Kang, S. J.; Yoo, K.-H.; Whang, C. N.; Moewes, A.; Chang, G. S. *J. Chem. Phys.* **2007**, *126*, 064706.

(17) Kang, S. J.; Yi, Y.; Kim, C. Y.; Yoo, K.-H.; Moewes, A.; Cho, M. H.; Denlinger, J. D.; Whang, C. N.; Chang, G. S. *Phys. Rev. B* **2005**, *72*, 205328.

(18) Skytt, P.; Guo, J.; Wassdahl, N.; Nordgren, J.; Luo, Y.; Ågren, H. *Phys. Rev. A* **1995**, *52*, 3572−3576.

(19) Watkins, N. J.; Gao, Y. *J. Appl. Phys*. **2003**, *94*, 1289−1291.

(20) Zhang, Z.-L.; Jiang, X.-Y.; Xu, S.-H.; Nagatomo, T.; Omoto, O. *J. Phys. D: Appl. Phys.* **1998**, *31*, 32−35.